

Fuel  
Manuscript Draft

Manuscript Number: JFUE-D-17-00739

Title: Digital coal: integrating micrometre to centimetre length scales

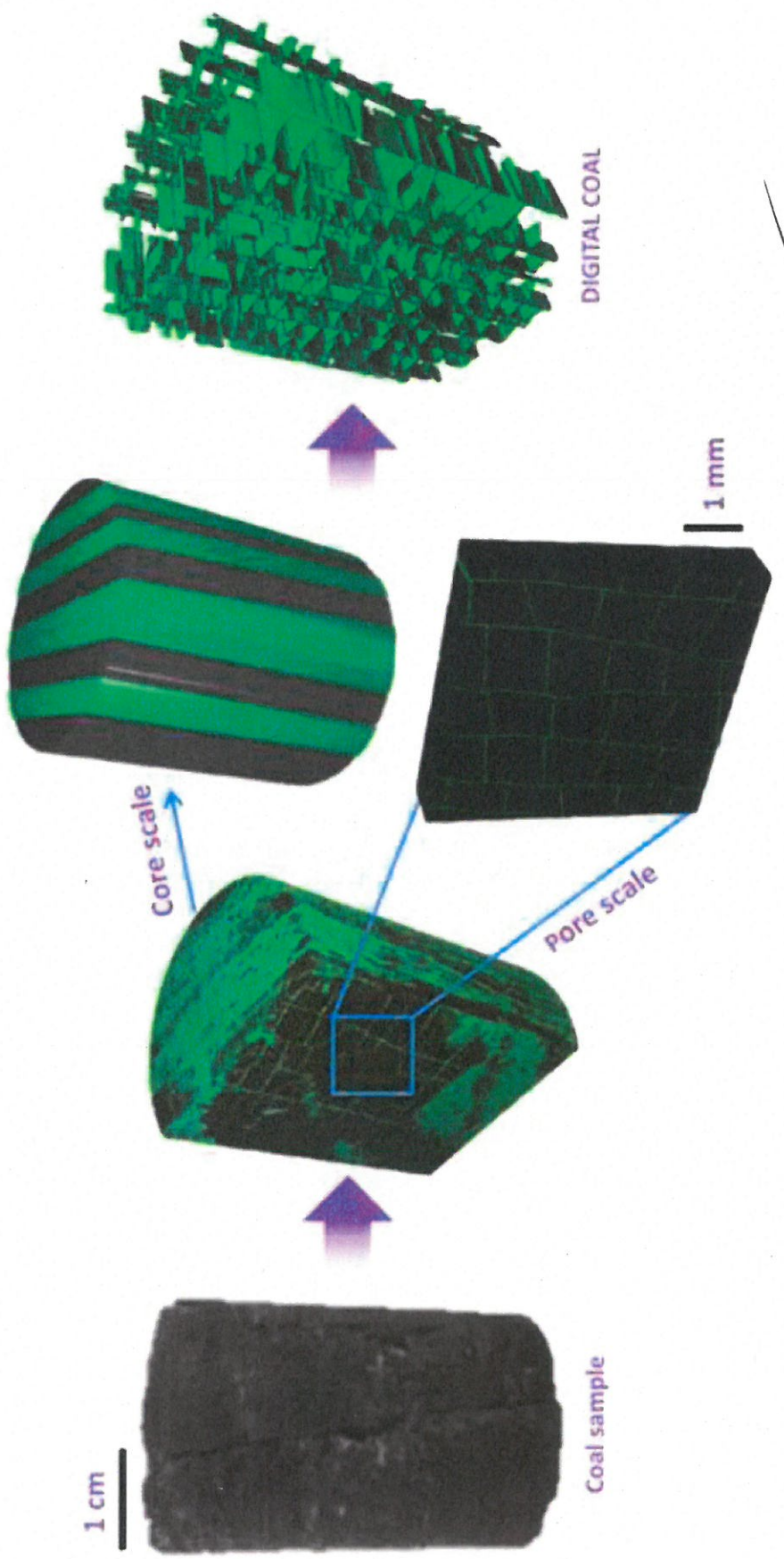
Article Type: Research paper

Keywords: Coal seam gas, micro-CT imaging, digital coal model, lithotypes, dull band, bright band, cleats, geometrical statistics

Abstract: Coal is highly heterogeneous at multiple scales, such that the characterisation of coal lags behind that of conventional reservoir rocks. This paper demonstrates the capability of a digital coal model that can be used to characterise the multiscale structure of coal as well as the petrophysical properties at the core scale (cm). X-ray micro-computed tomography (micro-CT) is applied to obtain the internal cleat structure of a heterogeneous coal sample, based on which statistics of coal lithotype distributions and cleat geometrical properties are extracted. Digital coal models are constructed stochastically according to the measured statistics. Resulting models preserve the core scale (cm) heterogeneity and pore scale ( $\mu\text{m}$  to mm) cleat properties of the imaged coal sample. Furthermore, petrophysical evaluation is performed based on stochastic digital coal models. We find that the generated digital coal models can provide permeability estimation with errors of 26.7% in comparison to that of the original micro-CT data. The presented model provides an alternative to the direct numerical simulation on segmented micro-CT images. The digital coal model is not restricted by image resolution, can be further extended in dimensions, and allows for the evaluation of coal heterogeneity and cleat structure.

## Highlights (for review)

- The band information of coal is numerically extracted from micro-CT data.
- A ‘digital coal’ model is developed to characterise coal multiscale heterogeneity. ✓
- Pore-scale features of cleats are integrated into core-scale digital coal model.
- Petrophysical properties of original micro-CT images are preserved by numerical models.



# 1      **Digital coal: integrating micrometre to centimetre 2      length scales**

3      **Yu Jing, Ryan T. Armstrong and Peyman Mostaghimi**

4      School of Petroleum Engineering, The University of New South Wales, NSW 2052, Australia

## 5      **Highlights**

- 6      • The band information of coal is numerically extracted from micro-CT data.
- 7      • A ‘digital coal’ model is developed to characterise coal multiscale heterogeneity.
- 8      • Pore-scale features of cleats are integrated into core-scale digital coal model.
- 9      • Petrophysical properties of original micro-CT images are preserved by numerical models.

## 10     **Abstract**

11    Coal is highly heterogeneous at multiple scales, such that the characterisation of coal lags behind that  
12    of conventional reservoir rocks. This paper demonstrates the capability of a digital coal model that  
13    can be used to characterise the multiscale structure of coal as well as the petrophysical properties at  
14    the core scale (cm). X-ray micro-computed tomography (micro-CT) is applied to obtain the internal  
15    cleat structure of a heterogeneous coal sample, based on which statistics of coal lithotype distributions  
16    and cleat geometrical properties are extracted. Digital coal models are constructed stochastically  
17    according to the measured statistics. Resulting models preserve the core scale (cm) heterogeneity and  
18    pore scale ( $\mu\text{m}$  to mm) cleat properties of the imaged coal sample. Furthermore, petrophysical  
19    evaluation is performed based on stochastic digital coal models. We find that the generated digital  
20    coal models can provide permeability estimation with errors of 26.7% in comparison to that of the  
21    original micro-CT data. The presented model provides an alternative to the direct numerical  
22    simulation on segmented micro-CT images. The digital coal model is not restricted by image  
23    resolution, can be further extended in dimensions, and allows for the evaluation of coal heterogeneity  
24    and cleat structure.

25    **Keywords:** Coal seam gas, micro-CT imaging, digital coal model, lithotypes, dull band, bright band,  
26    cleats, geometrical statistics

## 27     **1. Introduction**

28    Coal seam gas (CSG) is a valuable source of natural gas and is rapidly emerging around the world [1-  
29    3]. Compared with conventional gas reservoirs, coal is so permeated with methane that it can contain  
30    up to 7 times more methane than that of an equivalent size sandstone gas reservoir [4]. To efficiently  
31    recover this abundant energy, a detailed understanding of the fundamental properties of coal is  
32    required. CSG production is mainly controlled by coal permeability [3, 5], which is correlated to the  
33    coal fracture network, commonly known as “cleats”. The natural cleat system in coal spans a wide  
34    range of length scales, ranging from kilometre-length to nanometre-length scales [6]. X-ray micro-

35 computed tomography (micro-CT), a non-destructive imaging technology, can detect cleats at the  
36 micrometre-length scale, providing 3D images of a coal sample that is a few centimetres in diameter.  
37 Apart from cleats, micro-CT images can reveal the distribution of macerals and minerals [7].  
38 Petrophysical properties of coal are governed by the cleat geometrical properties, including  
39 orientation, length, spacing and aperture size [8].

40 Numerous researchers have used micro-CT imaging for acquiring coal geometric statistics [9-15].  
41 There are quantitative image analysis packages (e.g. Amira, QWIN, ImageJ, ICY) available for  
42 measuring cleat orientations, lengths and aperture sizes. The orientation measurement is based on  
43 calculating the largest eigenvector of the structure tensors [16, 17]. Lengths are determined by the  
44 number of voxels of skeletonised cleats. However, cleats intersecting with each other must be  
45 separated prior to these measurements, which requires manual editing and is less efficient for  
46 hundreds or thousands of cleats [13, 18]. Jing, Armstrong, Ramandi and Mostaghimi [14] have  
47 developed an automatic cleat-grouping algorithm to distinguish between face and butt cleats for  
48 subsequent image analysis, so that attributes of different cleat families can be analysed separately. In  
49 addition, aperture sizes are measured by placing 3D spheres inside cleats. The diameter of the sphere  
50 that fits inside is regarded as the aperture of the corresponding fracture [19]. Apart from that, cleat  
51 apertures can be measured from the CT number profiles that traverse a cleat [13, 20-22], where an  
52 obvious dip of the grey-scale profile indicates a cleat. Two parameters such as peak height (PH) and  
53 missing attenuation (MA) [23] of the profile are defined to calibrate with corresponding cleat  
54 apertures, thus apertures can be estimated according to the calibration curve. For coal samples, some  
55 cleats have aperture sizes below the micro-CT image resolution. Therefore, Ramandi, Armstrong and  
56 Mostaghimi [7] obtain high-resolution SEM images from coal surfaces and registers these images to  
57 the corresponding micro-CT data. Then a calibration curve is obtained by plotting attenuation  
58 coefficients against the measured aperture sizes from SEM images. Thus, the aperture size at each  
59 corresponding midpoint attenuation coefficient can be estimated.

60 Statistics measured from micro-CT data have been used for generating discrete fracture network  
61 models (DFN) [14, 15, 18, 24]. DFN models, consisting of discrete planes whose geometrical  
62 properties are statistically distributed, have been widely applied to characterise the cleat system for its  
63 ability of accounting for fracture geometrical properties explicitly [25-30]. Recently, Jing, Armstrong,  
64 Ramandi and Mostaghimi [14] have developed a novel DFN model for coal by applying statistics  
65 obtained from micro-CT data. The developed DFN model is comprised of two orthogonal sets of sub-  
66 parallel cleats: face cleats and butt cleats. The DFN algorithm mimics the cleat formation process,  
67 where face cleats form first and are extensive while butt cleats are generated later and terminate at  
68 face cleats, creating “T-junction” connections.

69 The well-organised cleat network pattern studied above mostly occurs in “bright bands” that are rich  
70 in vitrain material, which is brittle [31]. Bright bands have a bright lustre and are permeated with  
71 fractures at right angles [32]. However, coal is highly heterogeneous, comprising of multiple  
72 lithotypes [31, 33]. Apart from bright bands, coal that is composed of durian is called “dull bands”,  
73 where durian is a grey to black material with a dull lustre [32]. Most coal appear to be banded because  
74 of the alternating bright and dull bands [34, 35] which originate from different plant materials [31, 33].  
75 Unlike bright bands, dull bands have significantly different cleat properties: (1) dull bands do not  
76 have a systematic cleat network, where face and butt cleats are hardly recognised [34, 36]; (2) cleats  
77 of dull bands, named “dull cleats”, are poorly developed, appearing to be short, discontinuous and  
78 unidirectional [34]; (3) dull cleats have larger spacing than bright cleats [3, 37-39]. Dull cleats are

79 rarely observed in coal samples not only because they are generally rare, but also because the spacing  
80 of dull cleats is often larger than standard core samples [40]. As evident from these studies, different  
81 coal bands have unique cleat properties and thus, the characterisation of coal bands is of paramount  
82 importance.

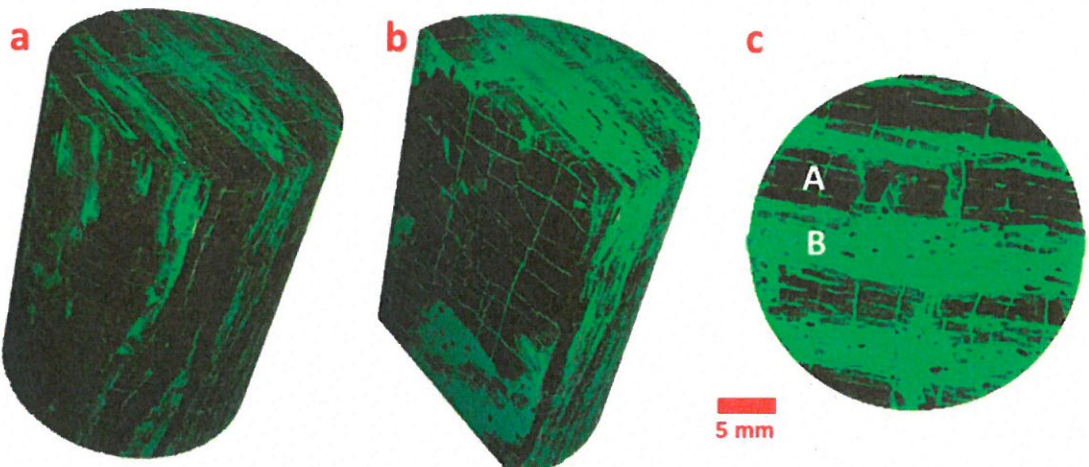
83 The DFN methods developed by Jing et al. (2016) focuses on a single lithotype at the pore scale (mm),  
84 which is unable to characterise multi-scale heterogeneity of coal. Such a model hinders the potential  
85 application for larger scale simulation. Therefore, we have developed a digital coal model at the core  
86 scale (cm), which not only incorporates pore-scale cleat geometrical properties but also preserves coal  
87 lithotype information. ] obj?

## 88 2. Material and Method

### 89 2.1. Sample Information

90 We use a coal sample collected from the Moura coal mine, Australia. Moura mine is a commercial  
91 CSG production site located on the southeast of Bowen Basin, Queensland [41]. Its CSG exploration  
92 and development is concentrated in seams around 200-500 m depth. The sample is 24 mm in diameter  
93 and 28.5 mm in length. It is a late Permian medium volatile bituminous coal, with vitrinite reflectance  
94 of 1.15%. The detailed sample specifications, including proximate and ultimate analyses are provided  
95 by Ramandi, Mostaghimi, Armstrong, Saadatfar and Pinczewski [42]. Alternating bright and dull  
96 lithotypes with approximately similar proportions can be visualised (Figure 1). ✓

97 A high-resolution, large-field, helical micro-CT scanning instrument developed at Australian National  
98 University [43] is used to evaluate the three-dimensional pore-scale structure of the sample. X-rays  
99 are emitted from a micro-focus source to probe the sample, and a detector is used to record a series of  
100 X-ray transmission radiographs at different viewing angles [44]. Then collected data are processed  
101 with a reconstruction algorithm [45] to provide a 3D micro-CT image that has a 16-bit grey-scale map  
102 represented by an array of voxels. The dimension of the resulting voxel array is 1504×1504×1780  
103 with a resolution of 16.5 μm. Image segmentation is then applied to partition the grey-scale image  
104 into unique phases, where the internal cleat network can be extracted for statistical analysis. ✓

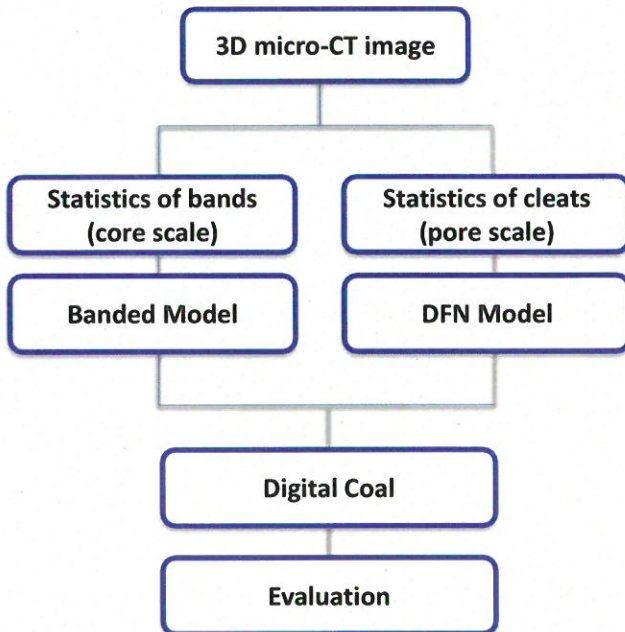


105

106 **Figure 1:** The coal sample with alternating bright and dull bands (a), where bright bands have  
 107 well-developed cleat networks with “T-junction” connections (b). The cross section of the coal  
 108 sample (c) shows that bright cleats cross the whole bright lithotype (A), while dull bands (B)  
 109 have few cleats developed.

110 **2.2. Methodology**

111 The first step is to extract statistic information of the coal sample by applying quantitative image  
 112 analysis processes. Distributions of bands and cleat geometric properties are acquired based on 3D  
 113 segmented micro-CT images, and further applied for constructing digital coal models stochastically.  
 114 Then, evaluation regarding the petrophysical and morphological properties of digital coal models is  
 115 conducted. Figure 2 provides an overview of the approach and the details of each step are discussed in  
 116 the following sections.



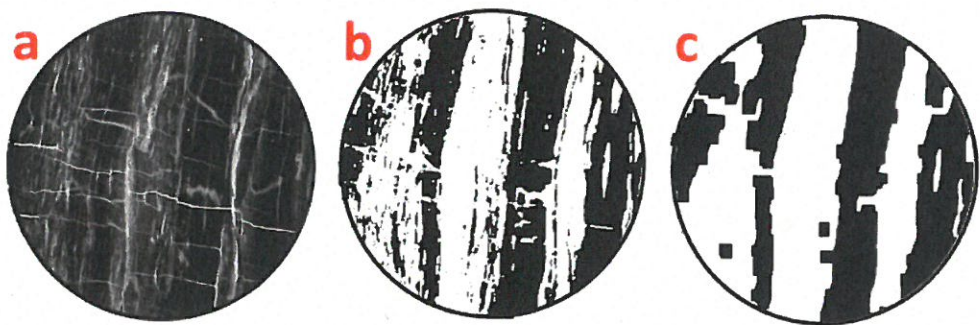
117

118     **Figure 2: Methodology workflow. Statistics of bands and cleat properties are measured from**  
119     **the segmented micro-CT images. Stochastic digital coal models are then constructed based on**  
120     **the measured statistic data using Monte Carlo method. Each digital coal realisation is evaluated**  
121     **and compared with original micro-CT images.**

122     2.3.       Statistics Acquisition

123     2.3.1.      Lithotype profiling

124     The key characteristic to distinguish different coal lithotypes is the brightness of coal, which  
125     corresponds to the amount of vitrinite. The sample was saturated with X-ray attenuation fluid and then  
126     images with micro-CT. The resulting image clearly displays the alternating bands that exist within the  
127     sample (Figure 3a). A low CT number (black color) identifies the bright bands whereas a high CT  
128     number (light grey color) identifies the dull bands. This distinction is possible due to the different  
129     degrees of micro porosity that exists within the different coal lithotypes. As bright and dull bands  
130     have a unique range of CT numbers, they can be quantified by the thresholding method [9-11, 46].  
131     Two cut-off values are defined according to visual inspection of the grey-scale image histogram.  
132     Voxels with grey values below the lower cut-off value are labelled as bright bands, and those between  
133     two cut-off values are labelled as dull bands. However, some microcleats have similar grey values  
134     with that of dull bands, thus erosion and dilation algorithms are further applied to separate cleats from  
135     the dull bands (Figure 3b). A binary lithotype profile is finally obtained (Figure 3c) for measuring  
136     band statistics, where the noisy spots below a minimum volume (the volume is set to be 200 voxels  
137     according to the band volume histogram) are removed from the statistical analysis.



138

139 **Figure 3: Lithotype profiling. (a) bright bands, dull bands and cleats have visual different grey**  
 140 **values; (b) after defining two cut-off values, the grey-scale image is converted to binary image;**  
 141 **(c) resulting lithotype profile is obtain by applying an eroding and dilating algorithm.**

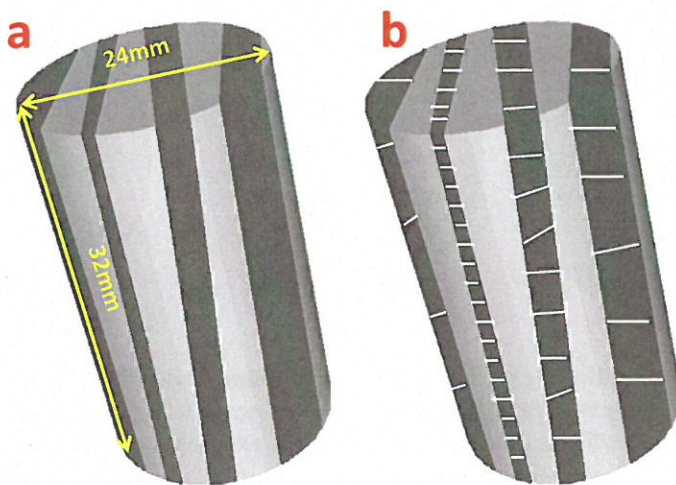
142 2.3.2. Quantitative Image Analysis

143 Based on the lithotype segmentation, band distributions are statistically analysed, including: (1)  
 144 volume fraction of bright bands; (2) average band thickness; and (3) band orientation. An edge  
 145 detector with Sobel approximation [47] is used to highlight the band boundaries, which returns edges  
 146 at those points with a maximum intensity gradient. The highlighted boundaries are then distinguished  
 147 between bright and dull band boundaries and subsequently measured for spacing and orientation. The  
 148 spacing between two boundaries of each band corresponds to the band thickness.

149 Bright cleats are extracted by overlaying the lithotype profiles onto the segmented micro-CT images.  
 150 Regions that overlap with bright bands will be of interests for statistical analysis. Geometric statistics  
 151 of bright cleats are measured by an automatic micro-CT image analysis method [14]. Prior to  
 152 measurements, an automatic cleat-grouping algorithm for bright cleats is utilised to distinguish  
 153 between face and butt cleats, which are used to extract independent statistics. Cleats of each 2D slice  
 154 of micro-CT data are first skeletonised to be one-voxel wide [48]. Each cleat-identified voxel is  
 155 tagged with 8 neighbours. Based on the direction in which the tagged cleat pixel extends, the cleats  
 156 are classified into either face cleat family or orthogonal butt cleat family. For the quantification of  
 157 cleat direction, the angle between the eigenvector with the largest eigenvalue of the structure tensor  
 158 towards the x-axis is measured, length refers to the number of voxels of each cleat in the skeletonised  
 159 image, spacing is the distance between the Cartesian voxel positions of adjacent cleats, and aperture  
 160 size is determined by the distance between two opposite cleat walls.

161 2.4. Construction of Digital Coal Models

162 The construction of core-scale digital coal models consists of two parts: (1) bright and dull bands  
 163 generation; and (2) integration of DFN models.

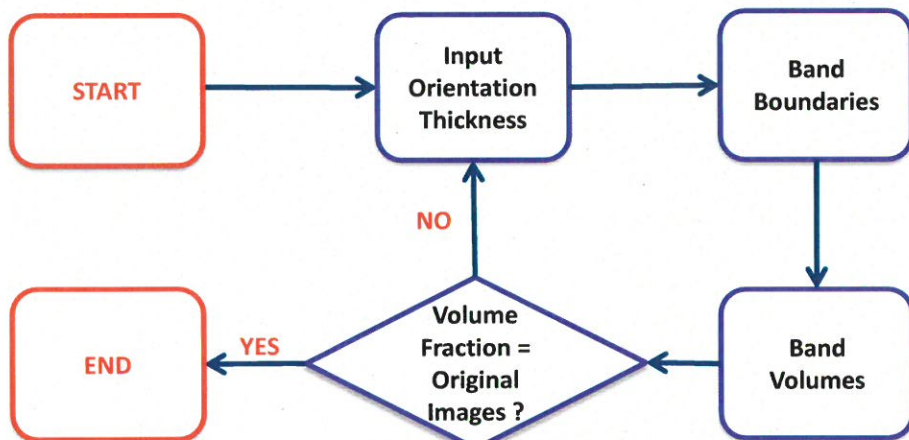


164

165 **Figure 4:** (a) The banded model where bright and dull bands are stochastically distributed over  
166 the sample; (b) bright cleats are reconstructed within the bright bands.

167 2.4.1. Band generation

168 A cylinder consisting of unit elements with the same dimensions of the original micro-CT images ( $D$   
169 = 1504 voxels,  $L$  = 1780 voxels) is generated first. Based on the measured thickness and orientation  
170 statistics, bright and dull bands are stochastically layered within the model (Figure 4a). This is  
171 realised by generating boundaries of each band, then a region-filling algorithm is applied to fill the  
172 volume between two boundaries. The procedure is repeated until the volume fraction of bright bands  
173 satisfies the value measured from the micro-CT data with allowed error (5%). Lastly, the thickness  
174 and orientation of each bright band is stored for further use. The overall workflow for band generation  
175 is illustrated in Figure 5.



176

177 **Figure 5:** Illustration of band generation workflow. Bright and dull bands are stochastically  
178 generated based on the thickness and orientation statistics. The procedure is repeated until the  
179 volume fraction of bright bands satisfies the value measured from the micro-CT data.

180 2.4.2. Integration of DFN models

181 Cleat networks are reconstructed in the bright bands of the banded model. According to the properties  
182 of bright cleats, they are well developed and organised, where face cleats and orthogonal butt cleats  
183 exhibit “T-junction” patterns. Jing, Armstrong, Ramandi and Mostaghimi [14] have developed a DFN  
184 modelling method specifically for bright cleats, which not only accounts for the geometrical statistics  
185 but also reproduces the particular cleat network pattern. To integrate DFN models with the banded  
186 model, the orientation of each bright band is used to calibrate the orientation of bright cleats so that  
187 both face and butt cleats are perpendicular to the bedding plane. In addition, based on the thickness of  
188 bright bands, corresponding statistical data are chosen for DFN modelling because spacing values  
189 vary with band thickness [38, 39, 49, 50]. Ramandi, Mostaghimi, Armstrong, Saadatfar and  
190 Pinczewski [42] quantified the effect of coal lithotypes on permeability based on the same sample  
191 studied herein. They considered 45 coal subsets (approximately 5.6 mm<sup>3</sup>) from bright and dull bands,  
192 and computed the permeability. It was found that the permeability of dull band subsets are 3–4 orders  
193 of magnitude lower than that of the bright band subsets. The results were explained by the observation  
194 that the cleats of dull bands were poorly connected. Therefore, we assume that the permeability of  
195 dull bands in comparison with bright bands can be ignored, so that cleats are not constructed in the  
196 dull bands.

197 2.5. Evaluation of Digital Coal Models

198 2.5.1. Petrophysical Properties

199 The porosity and permeability of the resulting digital coal models are calculated to evaluate the  
200 consistence of the models over multiple realizations and comparison to the original micro-CT data.  
201 Porosity is simply determined by the fractional number of cleat voxels to the total number of voxels.  
202 The image-based measurement is highly dependent on the model resolution, which is equivalent to the  
203 original micro-CT data resolution. In a previous study, it was found that an image resolution of  
204 16.5 μm is sufficient for obtaining accurate porosity with less than 15% error [42].

205 Permeability is obtained by solving the Laplace equation using a finite element method,

$$\nabla \cdot \omega \nabla P = 0$$

206 where  $\omega$  is a voxel-based local conductivity measured from the Euclidean distance map of the pore  
207 phase and  $P$  is pressure [51]. Neumann boundary condition is applied on the solid surfaces. The  
208 Laplace solver has been found to be suitable for fractured media where fractures have narrow widths  
209 that can result in numerical instabilities [7, 52, 53]. To compare the petrophysical results between the  
210 digital coal models and original images, the same numerical method and boundary conditions are used  
211 for both data sets.

212 2.5.2. Specific Surface Area

213 Another significant parameter studied in this work is the specific surface area (SSA). It refers to the  
214 total surface area per bulk volume (mm<sup>-1</sup>). For prediction of coal seam gas production, SSA is a

215 dominant parameter that affects gas sorption and transport in coal [54, 55]. For binary images, the  
216 SSA of the cleat network is determined by counting the surfaces of fracture-identified voxels that are  
217 exposed to solid-void boundaries. For each fracture-identified voxel (value = 0), it is revalued with the  
218 sum of the six neighbour voxels. Therefore, voxels that contact with matrix-identified voxels (value =  
219 1) will be revalued, while those totally inside void cleat space will remain zero. Lastly, total surface  
220 area is determined by dividing the sum of fracture-identified voxel values by total number of voxels.

221 2.5.3. Euclidean Distance Transform

222 The Euclidean distance map is calculated to analyse the geometry of the cleat network, which  
223 measures the distance from any voxel inside the cleats to the nearest void-solid boundary [56]. In  
224 three dimensions the Euclidean distance between  $P(x_1, y_1, z_1)$  and  $Q(x_2, y_2, z_2)$  is defined by,

$$d(P, Q) = \sqrt{(x_1 - x_2)^2 + (y_1 - y_2)^2 + (z_1 - z_2)^2}$$

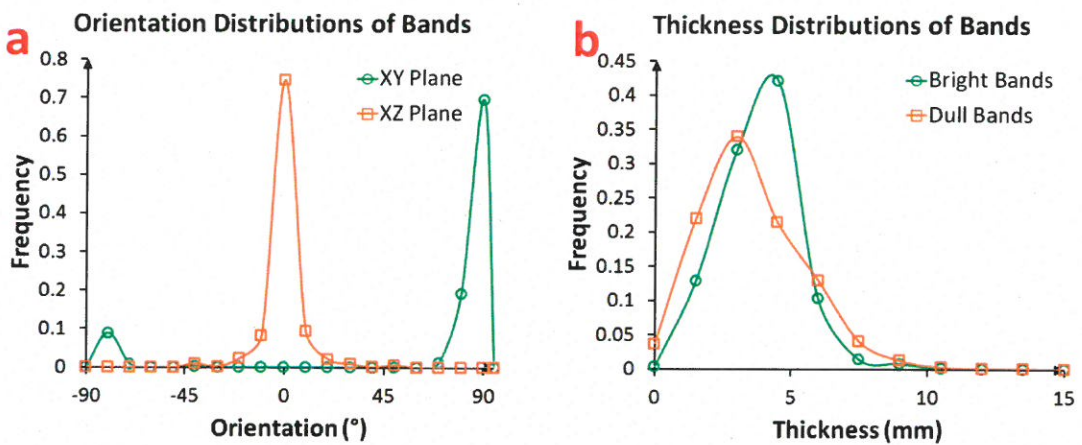
225 As a result, a 3D distance map where each voxel has a value equal to its Euclidean distance to the  
226 nearest boundary is generated. Therefore, the Euclidean distance map quantifies the geometry of the  
227 cleat network, which in turn influence transport properties, e.g. permeability [57].

228 **3. Results and Discussion**

229 3.1. Measured Statistical Results

230 1) Bands

231 Figure 6 shows the distributions of band orientation and thickness. It is shown from the orientation  
232 distribution that both bright bands and dull bands are nearly parallel with each other, and expand  
233 along the direction of the sample length. However, the bright bands of this sample are observed to be  
234 thicker than dull bands in general. In addition, the volume fraction of bright bands is measured to be  
235 52.4%, which is in agreement with Ramandi, Mostaghimi, Armstrong, Saadatfar and Pinczewski [42]  
236 that the coal sample contains approximately similar proportions of bright and dull lithotypes.



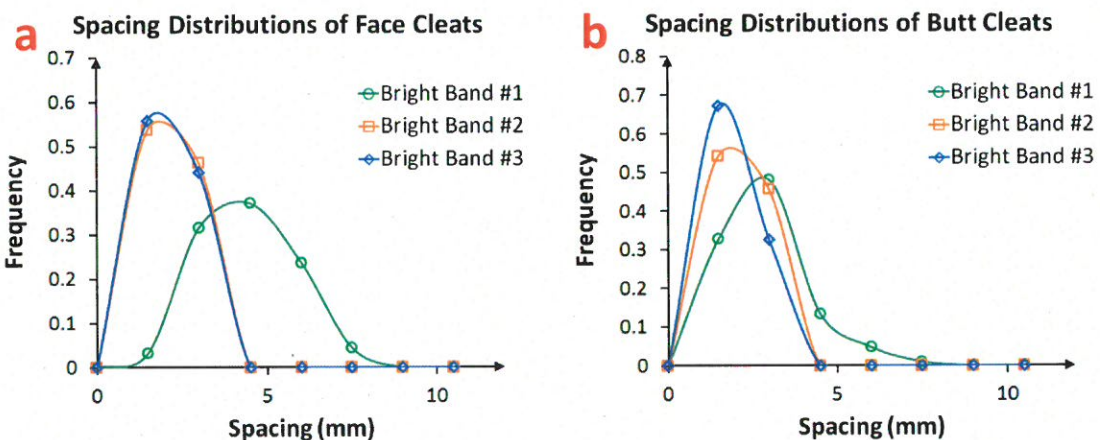
237

238 **Figure 6: Statistics of band orientation (a) and thickness (b).** It can be seen that: (1) both bright  
239 bands and dull bands are nearly parallel with each other, and expand along the direction of the  
240 sample length; (2) the bright bands of this sample are observed to be thicker than dull bands in  
241 general.

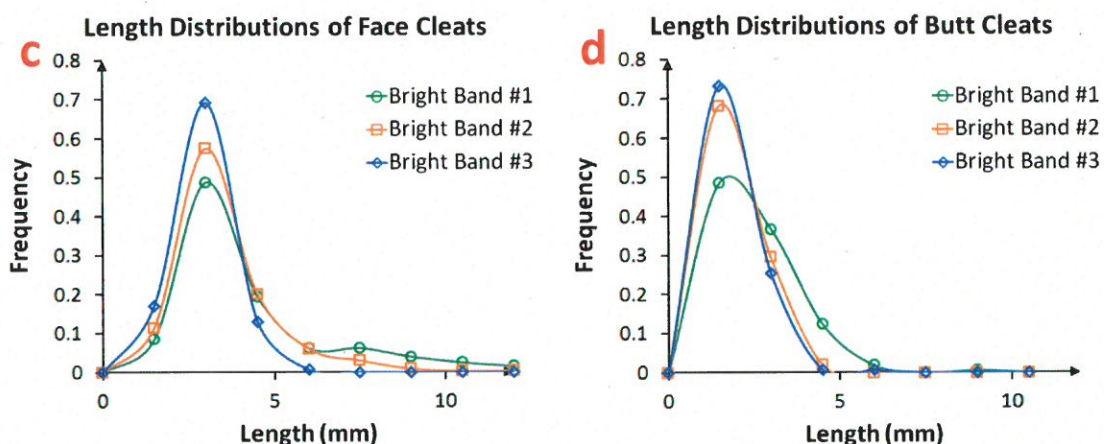
## 242 2) Bright Cleats

243 Three bright bands (Bright Band #1, #2, and #3) are extracted for property measurements, with  
244 average thicknesses of 9.28mm, 2.72mm and 1.76mm, respectively. Distributions of geometrical  
245 properties measured from three bright bands are shown in Figure 7. For the spacing distribution  
246 (Figure 7a & b), Bright Band #1 which has the largest thickness has the largest spacing distribution,  
247 while the thinnest Bright Band #3 is the most closely fractured. This is in agreement with findings of  
248 [38, 39, 49, 50], where average spacing is found to be linearly proportional to coal band thickness.  
249 Also, the face cleats of Bright Band #2 and #3 are more similarly spaced compared with the butt  
250 cleats, so the thickness-spacing relationship is more obvious in butt cleats. Due to the fact that butt  
251 cleats terminate at face cleats, the length of butt cleats will correspond to the face cleats spacing. Thus,  
252 similar phenomenon is observed in the length distribution of butt cleats (Figure 7d). For aperture  
253 distributions, it is shown that the aperture size is also influenced by the band thickness, especially for  
254 face cleats (Figure 7e & f), which is consistent with the linear relationship of aperture and band  
255 thickness provided by Close and Mavor [39]. The orientation distributions (Figure 7g - 7j) indicate  
256 that face and butt cleats are distributed orthogonally and both are perpendicular to the bedding plane.  
257 In summary, both spacing and apertures size are functions of band thickness, where thicker bands tend  
258 to have cleats that are spaced further apart and have larger aperture sizes (Table 1).

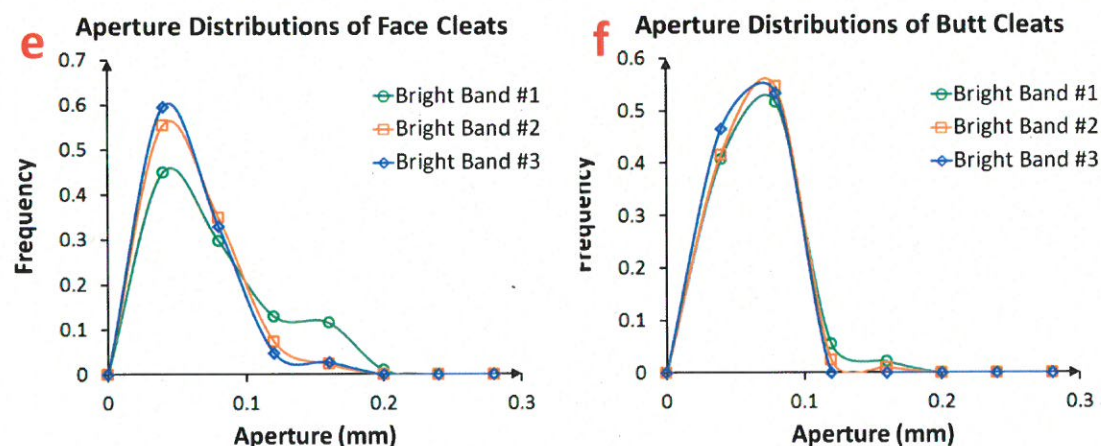
259



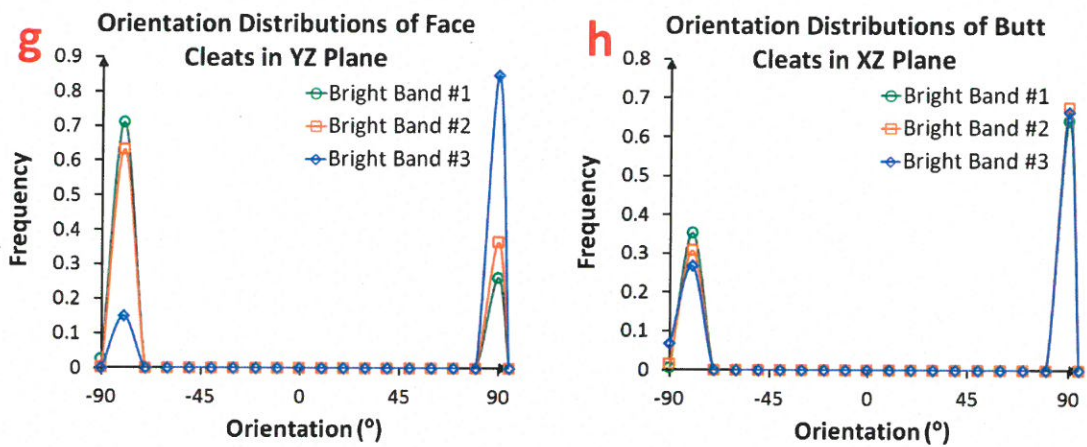
260



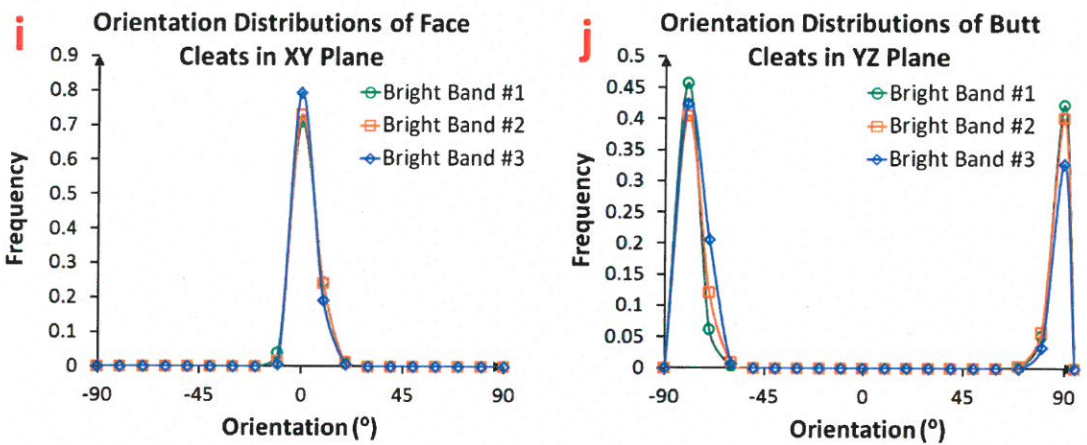
261



262



263



264

265 **Figure 7: Statistics of bright cleats: according to the spacing distribution (a-b), Bright Band #1**  
266 **(thickness = 9.28mm) has larger spacing than that of Bright Band #2 (thickness = 2.72mm)**  
267 **Bright Band #3 (thickness = 1.76mm). Similar phenomenon is shown in the length distribution**  
268 **of butt cleats (d), because butt cleat lengths correspond to the face cleats spacing. According to**  
269 **aperture statistics (e-f), thicker bands tend to have wider opened cleats. The orientation**  
270 **distributions (g-j) indicate that face and butt cleats are distributed orthogonal and both are**  
271 **perpendicular to the bedding plane.**

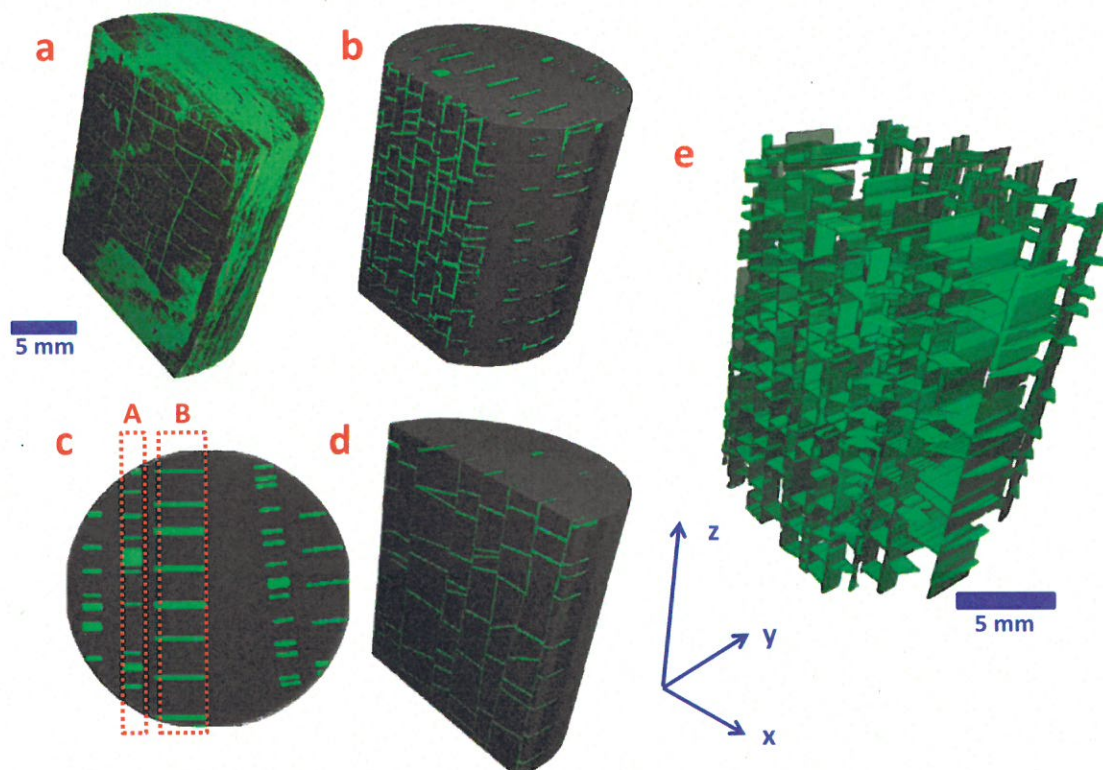
272 **Table 1: Comparison of averaged cleat spacing and aperture sizes between bright bands of**  
273 **different thicknesses**

Bright Band	Thickness [mm]	Spacing [mm]	Aperture [mm]
1	5.02	3.72	0.050
2	2.64	1.52	0.042
3	1.04	1.46	0.037

274

275     3.2.     Construction of Digital Coal Models

276     Based on our quantitative image analysis, digital coal models are constructed with configurations that  
277     are representative of the original micro-CT image, including dimension ( $D = 24\text{mm}$ ,  $L = 28.5\text{mm}$ ),  
278     resolution ( $16.5\mu\text{m}$ ) and bright band fractional volume (52.4%) as well as geometrical statistics.  
279     Figure 8 shows an example of a generated digital coal model. It is shown that the main structural  
280     features of the cleat network have been preserved. For example, the digital coal model consists of  
281     alternating bright and dull band with the same proportions of different lithotype bands. The bright  
282     bands are highly fractured while dull bands do not have a constructed cleat network, which are  
283     consistent with the observation from the real sample. By comparing the bright cleats of the original  
284     micro-CT data (Figure 8a) and digital coal models (Figure 8b & d), it can be seen that that the cleat  
285     pattern of bright cleats is preserved by the integrated DFN models. Furthermore, the relationship  
286     between cleat spacing and lithotype thickness is also realised by the representative digital coal  
287     modelling. Specifically, Figure 8b and Figure 8d present the cross sections extracted from Bright  
288     Band #A and #B shown in Figure 8c, respectively. As can be seen, Band #A is thinner than Band #B  
289     where the cleats are more closely spaced compared with those in band #B.



290

291     Figure 8: An example digital coal model of identical configurations with the original micro-CT  
292     data (a). (b) and (d) are two cross sections extracted from the Band #A and #B which are shown  
293     in (c). (e) is the total cleat network removed with coal matrix.

294      3.3.      Discussion

295      A total of 30 digital coal realisations are stochastically constructed with the Monte Carlo method [58].  
 296      The petrophysical properties and specific surface area (SSA) of all realisations and that of the original  
 297      micro-CT image are provided in Table 2. **Error! Reference source not found.** compares the  
 298      permeability of digital coal realisations with that of original micro-CT images. Circles represent the  
 299      permeability values of different digital coal models (ranging from 0.33D to 0.94D) whose average is  
 300      presented by the dashed line (0.59D), and the solid line is the permeability of the original micro-CT  
 301      images (0.46D). The results show that the permeability values of the digital coal models distribute  
 302      around the solid line with an error of 26.7% on average in comparison to the micro-CT data.

303      **Table 2: Computed results of digital coal models and original micro-CT images.**

Realisation Number	K [D]	$\phi$ [%]	SSA [mm <sup>-1</sup> ]
1	0.32	3.25	0.82
2	0.66	2.82	0.70
3	0.48	2.72	0.72
4	0.49	2.66	0.76
5	0.26	2.98	0.93
6	0.94	3.69	0.95
7	0.41	3.03	0.71
8	0.33	3.05	0.80
9	0.87	4.08	1.05
10	0.72	3.53	0.92
11	0.95	1.92	1.00
12	0.76	3.20	0.79
13	0.47	1.87	0.74
14	0.60	3.58	0.90
15	0.54	2.19	0.85
16	0.46	3.58	0.89
17	0.74	2.04	1.02
18	0.52	3.33	0.82
19	0.88	3.27	0.84
20	0.88	3.45	0.90
21	0.65	3.61	1.00
22	0.65	3.69	0.95
23	0.65	3.98	1.10
24	0.33	3.48	0.92
25	0.33	3.90	1.01
26	0.52	2.87	0.70
27	0.51	3.62	0.90
28	0.54	3.62	0.90
29	0.48	3.58	0.88
30	0.70	2.95	1.13
<b>Average Digital Coal Models</b>	0.59	3.18	0.89
<b>Original micro-CT Images</b>	0.46	7.12	3.30

PAGE NUMBERING  
Fy9 (p 15)  
&  
Fy9 (p 16)

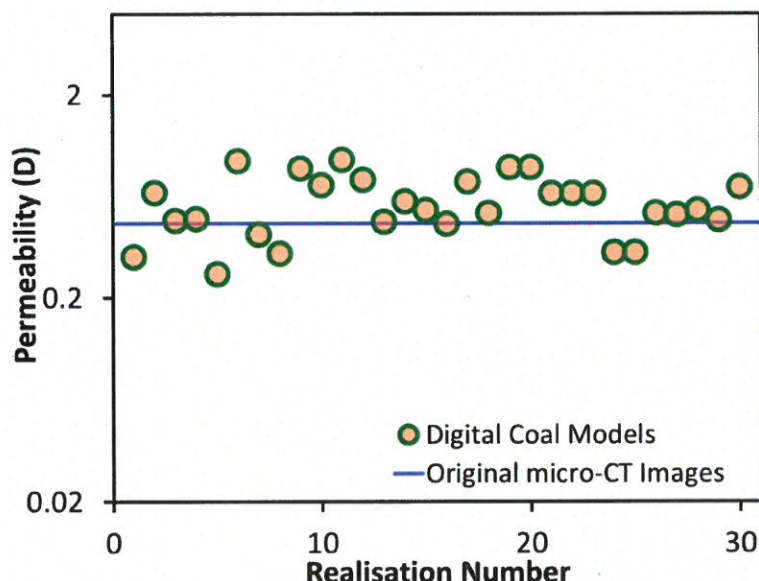
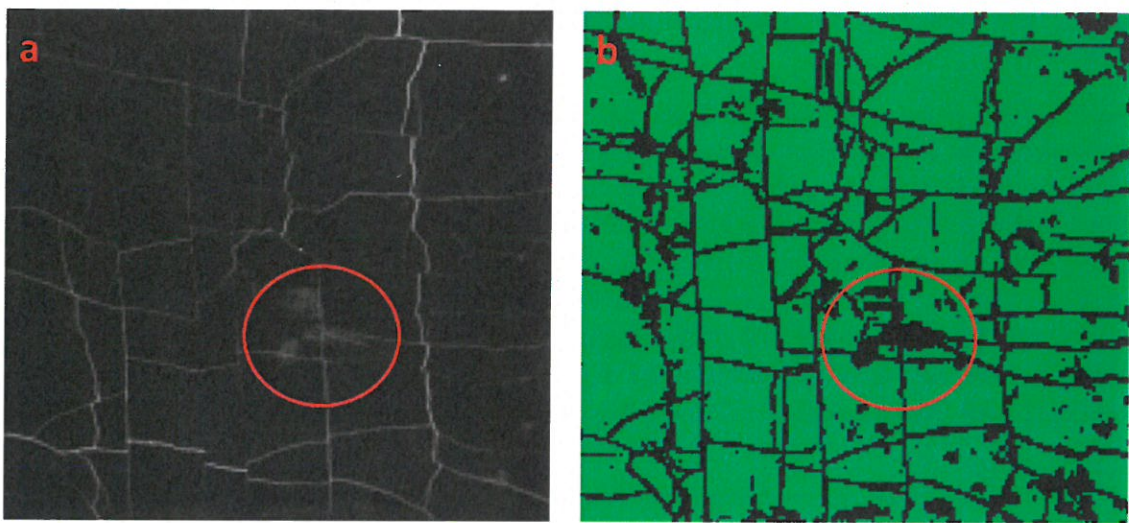


Figure 9: Comparison of permeability between digital coal models and the original micro-CT images. Permeability values estimated from the digital coal models (circles) is close to that of original micro-CT images (solid line). However, the average permeability (dashed line) is slightly overestimated.

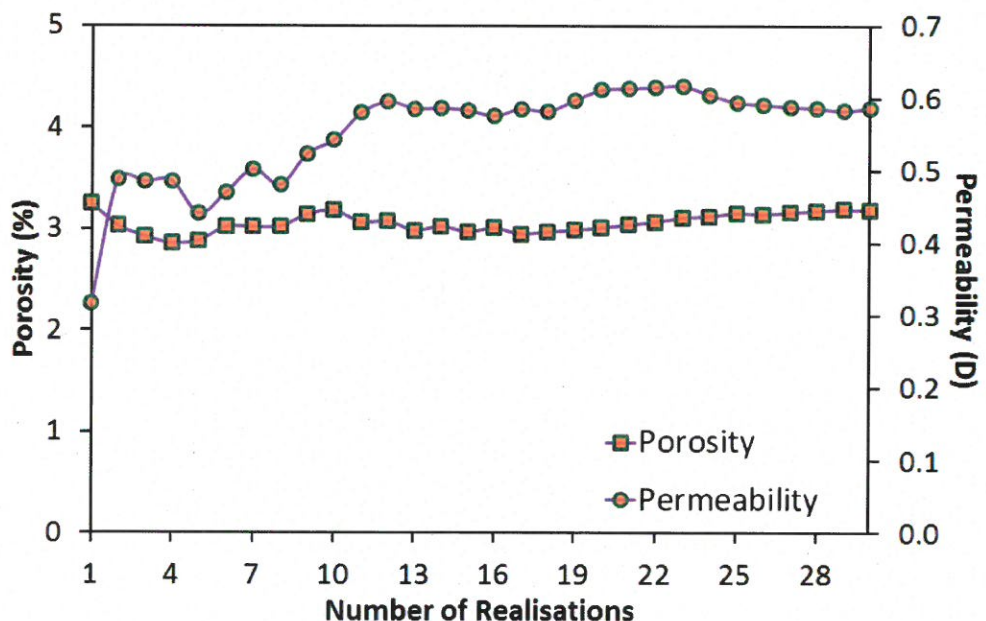
While the digital coal models provide reasonable permeability values in comparison to the original micro-CT data, both the porosity and specific surface area of the digital coal models (3.18% and  $0.89\text{mm}^{-1}$ , respectively) are lower than that of the original micro-CT data (7.12% and  $3.30\text{mm}^{-1}$ , respectively). We find that this is because of isolated short cleats and dead-end pores that exist in the original micro-CT image that are not included in the digital coal models. Another critical reason is related to image segmentation errors. Image segmentation is the most importance step affecting all subsequent quantitative analysis and modelling [59]. Common segmentation methods require a manually defined threshold value. However, the existence of noise hinders the correct determination of the threshold value, which can result in segmentation errors. Take an example of a sub-section from our original grey-scale image (Figure 9a), the noise (highlighted by a red circle) has similar grey values as those associate with cleats. As a result, the noise is mistakenly segmented to be void space in Figure 9b, which induces excessive porosity and specific surface area. However, digital coal models do not have these issues and thus could be providing a more accurate estimation of porosity and specific surface area.



324

325 **Figure 9:** A sub-section from the original grey-scale image (a) with noise (red circled). In  
 326 segmented image (b), the noise is segmented as void space which induces excessive porosity and  
 327 specific surface area.

328 The variations of average permeability and porosity as a function of the number of realisations are  
 329 plotted in Figure 10. As can be seen the variation of average permeability sharply decreases after 12  
 330 realisations, reaching a plateau of 0.59D approximately. Conversely, there is less of an effect of the  
 331 number of realisations on the porosity estimation, the porosity fluctuates slightly and stabilises at  
 332 around 3% after 10 realisations.

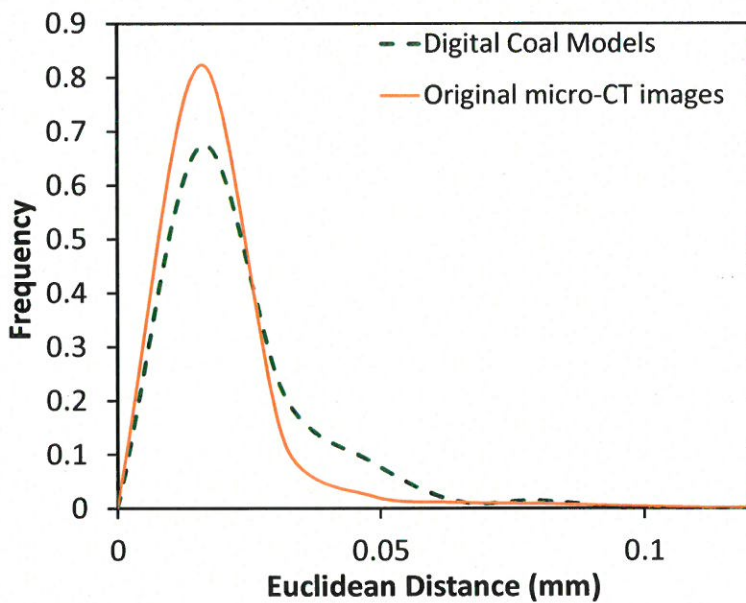


333

334 **Figure 10:** The variation of permeability and porosity as a function of the number of digital coal  
 335 realisations. After 12 realisation, the average permeability starts to be stable, reaching a plateau

336 of 0.59D approximately. Conversely, there is less of an effect of the number of realisations on  
337 the porosity estimation, the porosity fluctuates slightly and stabilises at around 3% after 10  
338 realisations.

339 The Euclidean distance maps of the digital coal models and the original miro-CT data are obtained  
340 and compared any geometrical differences. Figure 11 presents the frequency of Euclidean distance  
341 values for the cleats in the original micro-CT image and the average of the digital coal models. It is  
342 observed that the Euclidean distance distribution of both digital coal models and original micro-CT  
343 images peak at approximately 0.016mm. Thus, the digital coal models have geometries that are  
344 similar to that of the original micro-CT data. However, the Euclidean distance in the range from  
345 0.3mm to 0.7mm of the digital coal models accounts for higher probability than the original micro-CT  
346 data. This is because generated cleats of the digital coal models have smooth and parallel surfaces,  
347 while real cleats from the original micro-CT data have various opening widths and rough surfaces.



348

349 **Figure 11: Comparison of Euclidean distance histogram between digital coal models and**  
350 **original micro-CT images. It is shown that the Euclidean distance distribution of both digital**  
351 **coal models and original micro-CT images peak at approximately 0.016mm. Thus, the digital**  
352 **coal models have geometries that are similar to that of the original micro-CT data.**

#### 353 4. Conclusions

354 A novel core-scale digital coal model has been developed. The model not only characterises  
355 geometrical heterogeneity on multiple scales, but also preserves the petrophysical properties of  
356 segmented micro-CT data. The model incorporates band information at the core scale (cm) and cleat  
357 statistics at the pore scale (mm) from segmented coal micro-CT data. The developed digital coal  
358 models are found to be representative for the original micro-CT images with regards to petrophysical  
359 properties, providing reliable permeability estimation with an average error of 26.7%.

360 The digital coal models developed in this paper can be an alternative to the collection of micro-CT  
361 data, since digital coal models can address challenges that are inherent to micro-CT imaging and

362 segmentation. For example, our digital coal models can avoid segmentation-induced errors, such as  
363 the overestimation of specific surface area and porosity. Also, digital coal models are independent of  
364 image resolution as well as sample size. Instead of struggling with the trade-off between image  
365 resolution and domain size, digital coal models can provide digital representative images with desired  
366 resolution and extended dimensions to satisfy simulation requirements on larger scales. However,  
367 there are limitations in this work which will be the focus of our further work:

- 368     • Dull bands are assumed to impermeable where dull cleats are not constructed. Thus, porosity  
369       is underestimated based on the models because of the exclusion of dull cleats.  
370     • Master cleats which cross multiple bands are not included. More study of different cleat  
371       classes should be included.  
372     • Boundaries of bright and dull bands are assumed to be planar, while in reality bands have  
373       curved interfaces and may merge with each other. More complex band distribution is required  
374       for further digital coal models.  
375     • Real cleats have rough surfaces and variable opening widths, while cleats generated in digital  
376       coal models are assumed to have parallel and smooth walls. So characterisation of roughness  
377       is recommended.  
378     • The developed modelling method does not consider mineralisation, while the studied sample  
379       in this work has mineral fillings which have significant impacts on flow properties. So,  
380       mineralisation is recommended to be integrated in the further development of digital coal  
381       models.

382 **Reference**

- 383 [1] I. Hamawand, T. Yusaf, S.G. Hamawand, Coal seam gas and associated water: A review paper,  
384 Renewable and Sustainable Energy Reviews, 22 (2013) 550-560.
- 385 [2] C. Rodrigues, C. Laiginhas, M. Fernandes, M.L. de Sousa, M. Dinis, The coal cleat system: A new  
386 approach to its study, Journal of Rock Mechanics and Geotechnical Engineering, 6 (2014) 208-218.
- 387 [3] P.D. Gamson, B.B. Beamish, D.P. Johnson, Coal microstructure and micropermeability and their  
388 effects on natural gas recovery, Fuel, 72 (1993) 87-99.
- 389 [4] P. Thakur, S. Schatzel, K. Aminian, Coal bed methane: From prospect to pipeline, Elsevier, 2014.
- 390 [5] C. Pattison, C. Fielding, R. McWatters, L. Hamilton, Nature and origin of fractures in Permian coals  
391 from the Bowen Basin, Queensland, Australia, Geological Society, London, Special Publications, 109  
392 (1996) 133-150.
- 393 [6] H. Wang, Y. Yang, J. Yang, Y. Nie, J. Jia, Y. Wang, Evaluation of multiple-scale 3D characterization  
394 for coal physical structure with DCM method and synchrotron X-ray CT, The Scientific World Journal,  
395 2015 (2015).
- 396 [7] H.L. Ramandi, R.T. Armstrong, P. Mostaghimi, Micro-CT image calibration to improve fracture  
397 aperture measurement, Case Studies in Nondestructive Testing and Evaluation, 6 (2016) 4-13.

- 398 [8] P. Mostaghimi, R.T. Armstrong, A. Gerami, Y. Hu, Y. Jing, F. Kamali, M. Liu, Z. Liu, X. Lu, H.L.  
399 Ramandi, Cleat-scale characterisation of coal: An overview, *Journal of Natural Gas Science and*  
400 *Engineering*, 39 (2017) 143-160.
- 401 [9] F. Verhelst, P. David, W. Fermont, L. Jegers, A. Vervoort, Correlation of 3D-computerized  
402 tomographic scans and 2D-colour image analysis of Westphalian coal by means of multivariate  
403 statistics, *International Journal of Coal Geology*, 29 (1996) 1-21.
- 404 [10] F.J. Simons, F.d.r. Verhelst, R. Swennen, Quantitative characterization of coal by means of  
405 microfocal X-ray computed microtomography (CMT) and color image analysis (CIA), *International*  
406 *Journal of Coal Geology*, 34 (1997) 69-88.
- 407 [11] M. Van Geet, R. Swennen, Quantitative 3D - fracture analysis by means of microfocus X - Ray  
408 Computer Tomography ( $\mu$ CT): An example from coal, *Geophysical Research Letters*, 28 (2001) 3333-  
409 3336.
- 410 [12] C.O. Karacan, E. Okandan, Adsorption and gas transport in coal microstructure: investigation  
411 and evaluation by quantitative X-ray CT imaging, *Fuel*, 80 (2001) 509-520.
- 412 [13] S. Mazumder, K.-H. Wolf, K. Elewaut, R. Ephraim, Application of X-ray computed tomography for  
413 analyzing cleat spacing and cleat aperture in coal samples, *International Journal of Coal Geology*, 68  
414 (2006) 205-222.
- 415 [14] Y. Jing, R.T. Armstrong, H.L. Ramandi, P. Mostaghimi, Coal cleat reconstruction using micro-  
416 computed tomography imaging, *Fuel*, 181 (2016) 286-299.
- 417 [15] Y. Jing, R.T. Armstrong, P. Mostaghimi, Rough-walled discrete fracture network modelling for  
418 coal characterisation, *Fuel*, 191 (2017) 442-453.
- 419 [16] B. Jahne, *Spatio-Temporal Image Processing: Theory and Scientific Applications*, Springer-Verlag  
420 New York, Inc., 1993.
- 421 [17] J. Bigun, T. Bigun, K. Nilsson, Recognition by symmetry derivatives and the generalized structure  
422 tensor, *Pattern Analysis and Machine Intelligence, IEEE Transactions on*, 26 (2004) 1590-1605.
- 423 [18] D. Bossie-Codreanu, K.-H.A. Wolf, R. Ephraim, A new characterization method for coal bed  
424 methane, *Geologica Belgica*, 7 (2004) 37-145.
- 425 [19] R. Dougherty, K.-H. Kunzelmann, Computing local thickness of 3D structures with ImageJ,  
426 *Microscopy and Microanalysis*, 13 (2007) 1678-1679.
- 427 [20] R.A. Johns, J.S. Steude, L.M. Castanier, P.V. Roberts, Nondestructive measurements of fracture  
428 aperture in crystalline rock cores using X ray computed tomography, *Journal of Geophysical*  
429 *Research: Solid Earth (1978–2012)*, 98 (1993) 1889-1900.
- 430 [21] V. Muralidharan, D. Chakravarthy, E. Putra, D. Schechter, Investigating fracture aperture  
431 distributions under various stress conditions using X-ray CT scanner, in: *Canadian International*  
432 *Petroleum Conference*, Petroleum Society of Canada, 2004.
- 433 [22] K. Vandersteen, B. Busselen, K. Van Den Abeele, J. Carmeliet, Quantitative characterization of  
434 fracture apertures using microfocus computed tomography, *Geological Society, London, Special*  
435 *Publications*, 215 (2003) 61-68.

- 436 [23] R.A. Ketcham, D.T. Slottke, J.M. Sharp, Three-dimensional measurement of fractures in  
437 heterogeneous materials using high-resolution X-ray computed tomography, *Geosphere*, 6 (2010)  
438 499-514.
- 439 [24] M. Voorn, U. Exner, A. Barnhoorn, P. Baud, T. Reuschlé, Porosity, permeability and 3D fracture  
440 network characterisation of dolomite reservoir rock samples, *Journal of Petroleum Science and*  
441 *Engineering*, 127 (2015) 270-285.
- 442 [25] G. Baecher, N. Lanney, H. Einstein, Statistical description of rock properties and sampling, in: The 18th US Symposium on Rock Mechanics (USRMS), American Rock Mechanics Association, 1977.
- 444 [26] A. Robertson, The interpretation of geological factors for use in slope theory, in: Planning Open  
445 Pit Mines, Proceedings, Johannesburg, 1970, pp. 55-71.
- 446 [27] M. Cacas, E. Ledoux, G.d. Marsily, B. Tillie, A. Barbreau, E. Durand, B. Feuga, P. Peaudecerf,  
447 Modeling fracture flow with a stochastic discrete fracture network: Calibration and validation: 1. The  
448 flow model, *Water Resources Research*, 26 (1990) 479-489.
- 449 [28] N. Deisman, D.M. Ivars, C. Darcel, R.J. Chalaturnyk, Empirical and numerical approaches for  
450 geomechanical characterization of coal seam reservoirs, *International Journal of Coal Geology*, 82  
451 (2010) 204-212.
- 452 [29] L. Scholtès, F.-V. Donzé, M. Khanal, Scale effects on strength of geomaterials, case study: coal,  
453 *Journal of the Mechanics and Physics of Solids*, 59 (2011) 1131-1146.
- 454 [30] F. Gao, D. Stead, H. Kang, Numerical investigation of the scale effect and anisotropy in the  
455 strength and deformability of coal, *International Journal of Coal Geology*, 136 (2014) 25-37.
- 456 [31] R.R. Dutcher, *Field Description Of Goal*, Astm International, 1978.
- 457 [32] M.C. Stopes, On the four visible ingredients in banded bituminous coal: studies in the  
458 composition of coal, No. 1, *Proceedings of the Royal Society of London. Series B, Containing Papers*  
459 *of a Biological Character*, 90 (1919) 470-487.
- 460 [33] S.R. Dindarloo, A. Bagherieh, J.C. Hower, J.H. Calder, N.J. Wagner, Coal modeling using Markov  
461 Chain and Monte Carlo simulation: Analysis of microlithotype and lithotype succession, *Sedimentary*  
462 *Geology*, 329 (2015) 1-11.
- 463 [34] W. Riese, W.L. Pelzmann, G.T. Snyder, New insights on the hydrocarbon system of the Fruitland  
464 Formation coal beds, northern San Juan Basin, Colorado and New Mexico, USA, *Geological Society of*  
465 *America Special Papers*, 387 (2005) 73-111.
- 466 [35] R.M. Flores, *Coal and coalbed gas: fueling the future*, Newnes, 2013.
- 467 [36] G. Dawson, J. Esterle, Controls on coal cleat spacing, *International Journal of Coal Geology*, 82  
468 (2010) 213-218.
- 469 [37] S. Weniger, P. Weniger, R. Littke, Characterizing coal cleats from optical measurements for CBM  
470 evaluation, *International Journal of Coal Geology*, 154–155 (2016) 176-192.

- 471 [38] C.M. Tremain, S.E. Laubach, N.H. Whitehead III, Coal fracture (cleat) patterns in Upper  
472 Cretaceous Fruitland formation, San Juan Basin, Colorado and New Mexico-implications for coalbed  
473 methane exploration and development, (1991).
- 474 [39] J.C. Close, M.J. Mavor, Influence of Coal Composition and Rank on Fracture Development in  
475 Fruitland Coal Gas Reservoirs of San Juan Basin, in: Assoc. Geol. Field Conf, Coalbed Methane of  
476 Western North America, Rk. Mt., 1991, pp. 109-121.
- 477 [40] J. Esterle, Y. Kolatschek, G. O'Brien, Relationship between in situ coal stratigraphy and particle  
478 size and composition after breakage in bituminous coals, International journal of coal geology, 49  
479 (2002) 195-214.
- 480 [41] A.L. Dicks, J.C. Diniz da Costa, A. Simpson, B. McLellan, Fuel cells, hydrogen and energy supply in  
481 Australia, Journal of Power Sources, 131 (2004) 1-12.
- 482 [42] H.L. Ramandi, P. Mostaghimi, R.T. Armstrong, M. Saadatfar, W.V. Pinczewski, Porosity and  
483 permeability characterization of coal: a micro-computed tomography study, International Journal of  
484 Coal Geology, 154–155 (2016) 57-68.
- 485 [43] A. Sheppard, S. Latham, J. Middleton, A. Kingston, G. Myers, T. Varslot, A. Fogden, T. Sawkins, R.  
486 Cruikshank, M. Saadatfar, Techniques in helical scanning, dynamic imaging and image segmentation  
487 for improved quantitative analysis with X-ray micro-CT, Nuclear Instruments and Methods in Physics  
488 Research Section B: Beam Interactions with Materials and Atoms, 324 (2014) 49-56.
- 489 [44] T. Varslot, A. Kingston, G. Myers, A. Sheppard, High-resolution helical cone-beam micro-CT with  
490 theoretically-exact reconstruction from experimental data, Medical physics, 38 (2011) 5459-5476.
- 491 [45] J. Hsieh, Computed tomography: principles, design, artifacts, and recent advances, in, SPIE  
492 Bellingham, WA, 2009.
- 493 [46] Y. Yao, D. Liu, Y. Che, D. Tang, S. Tang, W. Huang, Non-destructive characterization of coal  
494 samples from China using microfocus X-ray computed tomography, International Journal of Coal  
495 Geology, 80 (2009) 113-123.
- 496 [47] I. Sobel, An isotropic 3× 3 image gradient operator, Machine Vision for three-demensional  
497 Sciences, (1990).
- 498 [48] T.-C. Lee, R.L. Kashyap, C.-N. Chu, Building skeleton models via 3-D medial surface/axis thinning  
499 algorithms, CVGIP: Graph. Models Image Process., 56 (1994) 462-478.
- 500 [49] S. Laubach, R. Marrett, J. Olson, A. Scott, Characteristics and origins of coal cleat: a review,  
501 International Journal of Coal Geology, 35 (1998) 175-207.
- 502 [50] B. Law, The relationship between coal rank and cleat spacing: implications for the prediction of  
503 permeability in coal, in: Proceedings of the 1993 International Coalbed Methane Symposium,  
504 Twscaloosa, ALabma: University of ALabama, 1993.
- 505 [51] A.D. Khalili, C.H. Arns, J.-Y. Arns, F. Hussain, Y. Cinar, W.V. Pinczewski, S. Latham, J. Funk,  
506 Permeability upscaling for carbonates from the pore-scale using multi-scale Xray-CT images, in:  
507 SPE/EAGE European Unconventional Resources Conference & Exhibition-From Potential to  
508 Production, 2012.

- 509 [52] C.H. Arns, F. Baugé, A. Limaye, A. Sakellariou, T. Senden, A. Sheppard, R.M. Sok, V. Pinczewski, S.  
510 Bakke, L.I. Berge, Pore scale characterization of carbonates using X-ray microtomography, Spe  
511 Journal, 10 (2005) 475-484.
- 512 [53] S. Norouzi Apourvari, C.H. Arns, Image-based relative permeability upscaling from the pore scale,  
513 Advances in Water Resources, 95 (2015) 161-175.
- 514 [54] J. Thomas, H.H. Damberger, Internal surface area, moisture content, and porosity of Illinois  
515 coals: Variations with coal rank, Circular no. 493, (1976).
- 516 [55] Z. Zhao, B. Li, Y. Jiang, Effects of Fracture Surface Roughness on Macroscopic Fluid Flow and  
517 Solute Transport in Fracture Networks, Rock Mechanics and Rock Engineering, 47 (2014) 2279.
- 518 [56] L. Chen, H.Y.H. Chuang, An efficient algorithm for complete Euclidean distance transform on  
519 mesh-connected SIMD, Parallel Computing, 21 (1995) 841-852.
- 520 [57] Z. Jiang, K. Wu, G. Couples, M. Van Dijke, K. Sorbie, J. Ma, Efficient extraction of networks from  
521 three - dimensional porous media, Water Resources Research, 43 (2007).
- 522 [58] S.H. Chen, X.M. Feng, S. Isam, Numerical estimation of REV and permeability tensor for  
523 fractured rock masses by composite element method, International journal for numerical and  
524 analytical methods in geomechanics, 32 (2008) 1459-1477.
- 525 [59] P. Iassonov, T. Gebrenegus, M. Tuller, Segmentation of X - ray computed tomography images of  
526 porous materials: A crucial step for characterization and quantitative analysis of pore structures,  
527 Water Resources Research, 45 (2009).

528

